separations

MDPI

Article

Application of Magnetic Aquatic Plant Biochar for Efficient Removal of Antimony from Water: Adsorption Properties and Mechanism

Luyi Nan [1,2], Yuting Zhang [1,2], Min Liu [1,2], Liangyuan Zhao [1,2,3,*], Yuxuan Zhu [1,2] and Xun Zhang [1,2]

[1] Basin Water Environmental Research Department, Changjiang River Scientific Research Institute, Wuhan 430010, China; 15537581677@163.com (L.N.); zyuting0806@163.com (Y.Z.); liumin_xl@126.com (M.L.); yuxuan_zhu1213@163.com (Y.Z.); 13971873360@163.com (X.Z.)
[2] Key Lab of Basin Water Resource and Eco-Environmental Science in Hubei Province, Wuhan 430010, China
[3] Innovation Team for Basin Water Environmental Protection and Governance of Changjiang Water Resources Commission, Wuhan 430010, China
* Correspondence: zhaoliangyuannew@163.com

Abstract: Antimony (Sb) pollution in natural water bodies can cause significant harm to aquatic ecosystems. Currently, the utilization of chemicals in water bodies presents disadvantages, such as the hardship in collecting dispersed flocs and the incomplete elimination of pollutants. In the present research, a novel type of efficient adsorbent material for the magnetic recovery of Sb was proposed: the magnetic aquatic plant biochar. Its adsorption characteristics and mechanism were deeply investigated. The results demonstrated that, among the three types of aquatic plants, the magnetic biochar of Arundo donax magnetic biochar (LMBC) displayed the most superior adsorption effect on Sb. Under optimal adsorption conditions (pyrolysis temperature of 300 °C, dosage of 100 mg, pH of 8), the removal rate of Sb by LMBC exceeded 97%. The adsorption rate of Sb by LMBC was relatively rapid, and the kinetics of adsorption conformed to a pseudo-second-order kinetic model. The adsorption isotherm was consistent with the Langmuir and Freundlich models, and the maximum adsorption capacity of Sb reached 26.07 mg/g, suggesting that the adsorption process pertained to the adsorption of multi-molecular layers. The influence of coexisting ions on the adsorption effect of LMBC was insignificant. The SEM characterization results revealed that LMBC mainly consisted of the elements C and O. The BET characterization results demonstrated that the magnetization modification augmented the specific surface area by approximately 30 times to reach 89.14 m^2/g, and the pore volume increased by twofold to 0.18 cm^3/g, creating a favorable condition for Sb adsorption. The FTIR, XRD, and XPS results indicated that the surface of LMBC was rich in carboxyl and hydroxyl groups and was successfully loaded with Fe_2O_3 and Fe_3O_4. LMBC not only facilitates the resourceful utilization of aquatic plant waste but also effectively removes antimony (Sb) pollution through its magnetic properties. This dual functionality presents promising application prospects for the efficient adsorption and removal of Sb from water.

Keywords: antimony pollution; aquatic plants; biochar; magnetic biochar

check for updates

Academic Editor: Mingheng Li

Received: 4 December 2024
Revised: 19 December 2024
Accepted: 24 December 2024
Published: 28 December 2024

Citation: Nan, L.; Zhang, Y.; Liu, M.; Zhao, L.; Zhu, Y.; Zhang, X. Application of Magnetic Aquatic Plant Biochar for Efficient Removal of Antimony from Water: Adsorption Properties and Mechanism. *Separations* **2025**, *12*, 2. https://doi.org/10.3390/separations12010002

Copyright: © 2024 by the authors. Licensee MDPI, Basel, Switzerland. This article is an open access article distributed under the terms and conditions of the Creative Commons Attribution (CC BY) license (https://creativecommons.org/licenses/by/4.0/).

1. Introduction

Antimony (Sb) is a naturally occurring cuprophilic element. Research has shown that Sb exists in the aquatic environment in complex forms and exhibits a bioconcentration effect, which can lead to significant environmental pollution issues even at low concentrations [1]. However, Sb mining activities can cause serious water pollution in the surrounding areas.

For instance, an investigation was conducted to evaluate the fundamental chemical properties, ion concentrations, and pollution profiles of water bodies in a Hunan tin mine. This assessment included smelting wastewater, tailing bar percolation water, pit water from mining operations, and adjacent river waters. The findings revealed that Sb levels across all sampled waters exhibited considerable variation, with concentrations ranging from 4581 to 29,423 μg/L and an overall average of 10,068 μg/L [2]. An investigation into the downstream river samples from the Dachang Sb deposit in Guangxi was conducted to evaluate the presence of Sb. The study revealed that the concentrations of Sb in the 14 collected river samples exhibited significant variability, ranging from 59.1 μg/L to 213.8 μg/L, with an overall average concentration of 139.9 μg/L [3]. In Sardinia, Italy, uncontaminated water samples taken from the upstream section of a river flowing through an abandoned mining area showed an Sb content of 1.7 μg/L. In contrast, water sampled from the same river at a distance of 200 m downstream from the mining site contained an Sb concentration of 28 μg/L [4]. In Alaska, a river located near an Sb mine recorded remarkably high levels of Sb, reaching up to 720 μg/L; furthermore, even at a distance of 8 km downstream from the mine, extremely elevated concentrations remained detectable [5].

Even though natural water bodies typically contain less than 1 μg/L of Sb, the issue of Sb pollution in aquatic environments has worsened due to increasing human activities [6]. China's Environmental Quality Standard for Surface Water (GB 3838-2002) designates Sb as a non-conventional indicator, establishing a limit of 5 μg/L [7]. Currently, research on Sb pollution primarily focuses on highly concentrated industrial wastewater, which ranges from 100 to 200 mg/L. However, when sudden Sb pollution incidents occur in natural rivers, the concentration levels are relatively low (50–100 μg/L), and there is a scarcity of investigations addressing the treatment of Sb contamination in natural waters with such low concentrations.

Adsorption is distinguished among various methods for the removal of antimony (Sb) from water due to its high efficiency, low cost, and ease of operation. At present, the primary materials utilized for adsorbing Sb encompass polymeric iron, polymeric aluminum, and so on. Despite their effectiveness, these materials tend to generate dispersed flocculants within the aqueous environment, complicating recovery efforts and failing to achieve complete separation of pollutants. This situation can lead to adverse effects on the contaminated water body. Therefore, it is essential to develop a method that can thoroughly eliminate Sb pollutants from water through effective adsorption and recovery processes while providing technical support for addressing Sb pollution effectively. Biochar, an eco-friendly and economical adsorbent, is favored for its large surface area, high porosity, and substantial adsorption capacity [8]. Additionally, the presence of functional groups such as carboxyl, amino, and hydroxyl on biochar's surface enhances selective cation adsorption [9]. However, due to the small particle size of the biochar powder, which is relatively dispersed and difficult to be separated from the water body after the application, several studies have indicated that biochar may pose potential risks to aquatic environments. These risks include exacerbation of eutrophication, acceleration of pollutant migration, and inhibition of growth in aquatic organisms [10]. In order to improve recycling of biochar materials, magnetic modification of biochar has become a research hotpot [11]. Modification via Fe-doping technology serves as a straightforward and effective method to enhance biochar adsorbents by introducing additional adsorption sites, thereby improving their overall adsorption capacity [12]. Currently, the raw materials employed for the preparation of biochar mainly consist of wood, straw, coconut shell, and food waste. The organic waste resources mostly originate from terrestrial vegetation, and there are relatively few studies on the utilization of aquatic plants as raw materials for the preparation of magnetic biochar.

Aquatic plants, due to their widespread distribution, high biomass yield, and rapid growth rates, are considered appealing raw materials for the production of biochar [13]. Their substantial biomass content has been extensively utilized in water treatment and ecological restoration projects aimed at removing nitrogen and phosphorus, heavy metals, and other pollutants from aquatic environments [14]. Consequently, utilizing aquatic plants as feedstock for biochar not only yields environmentally friendly materials but also promotes the sustainable management of these plant-derived solid wastes [15].

At present, many researches have reported that biochar prepared from different aquatic plants can remove heavy metals. Common aquatic plants like Typha angustifolia and Eichhornia crassipes absorb heavy metal ions and improve water quality using trace elements released by their own rhizomes [15,16]. Arundo donax, a widespread emergent plant in China, is supposedly an ideal biochar source due to its extensive roots, high biomass, adaptability, and heavy metal tolerance [17,18]. The plant species used in this study were classified as waste plant materials, which have no negative impact on the surrounding environment. Furthermore, their utilization has largely solved the problem of resource utilization of waste plant materials.

In the present research, the Sb pollution issue was addressed through the treatment concept of "what comes from the water can be used in the water," and biochar and magnetic biochar were fabricated from Typha angustifolia, Eichhornia crassipes, and Arundo donax. The optimal adsorption conditions of Sb were explored under different influencing factors, such as aquatic plant species, pH, dosage, and ionic strength. The microscopic properties of biochar and magnetic biochar were further analyzed by SEM, EDS, BET, XRD, XPS, and VSM. The adsorption capacity of biochar for Sb was investigated by adsorption kinetics and adsorption isotherm experiments, and the adsorption mechanism was discussed. The research findings can offer a novel and feasible solution for the treatment of such environmental problems and also contribute to the development of aquatic plant waste resources.

2. Materials and Methods

2.1. Materials and Chemicals

Aquatic plant samples (Typha angustifolia, Eichhornia crassipes, and Arundo donax) were collected from the Baiquan Fuhe Wetland in Wuhan, Hubei Province, China. Antimony Standard Solution (Sb, GSB04-1748-2004) was purchased from Guobiao (Beijing) Testing and Certification Co., Ltd., Beijing, China. Sodium hydroxide (NaOH, AR), ferrous sulfate heptahydrate (FeSO4·7H2O, AR), ferric chloride hexahydrate (FeCl3·6H2O, AR), nitric acid (HNO3, GR), and sodium chloride (NaCl, AR) were purchased from Sinopharm Chemical Reagent Co., Ltd., Shanghai, China.

GR: Guaranteed Reagent with a purity of 99.8%, which is suitable for critical and precise analytical tasks as well as scientific research.

AR: Analytical Reagent with a purity of 99.7%, which is marginally lower in purity compared to the highest grade, and is appropriate for significant analytical tasks and general research.

2.2. Preparation of Biochar and Magnetic Biochar

Figure 1 depicts the whole biochar and magnetic biochar preparation procedure. To be specific, the collected aquatic plant samples were firstly pretreated by washing, cutting, and crushing to obtain aquatic plant powders with a particle size of 0.15 mm (100 mesh), then dried in an oven at 70 °C for 24 h and stored. Then, different kinds of aquatic plant powders were placed in a muffle furnace and calcined at 300 °C for 2 h to obtain the biochars, which were named Arundo donax biochar (LBC), Typha angustifolia biochar

(XBC), and Eichhornia crassipes biochar (FBC). The magnetic biochars were generated as follows. Firstly, nitrogen was continuously passed into a beaker containing 300 mL deionized water to drain all the oxygen, then 10 g $FeCl_3 \cdot 6H_2O$ and 5.56 g $FeSO_4 \cdot 7H_2O$ were added to make a mixed solution with Fe^{3+}:Fe^{2+} = 2:1. Next, 10 g biochar and 100 mL deionized water were added and stirred for 1 h, 1 mol/L NaOH solution was added to adjust the pH to 12, and then the beaker was transferred to a thermostat water bath at 70 °C and aged for 1 h. Finally, the suspension was centrifuged and the solid was separated and washed until the pH was neutral. Then, the solid was dried in an oven at 70 °C for 12 h to obtain the magnetic biochars, which were named Arundo donax magnetic biochar (LMBC), Typha angustifolia magnetic biochar (XMBC), and Eichhornia crassipes magnetic biochar (FMBC).

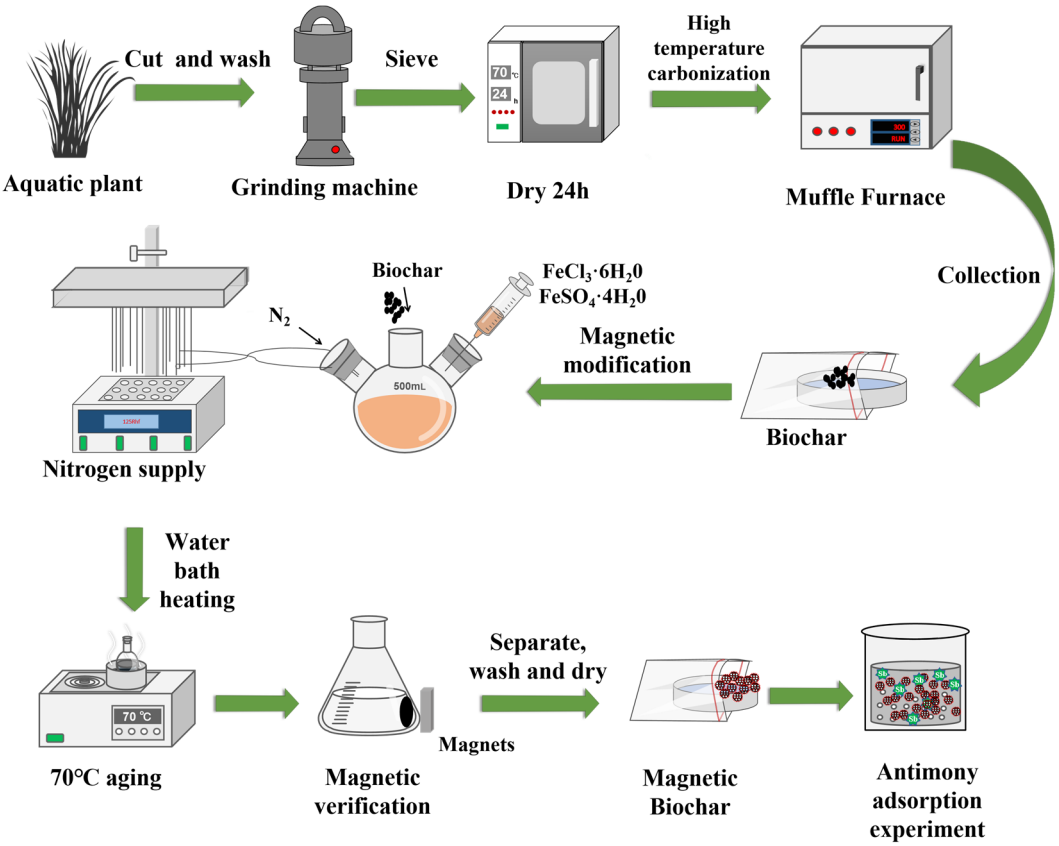


Figure 1. The preparation process of the biochars and magnetic biochars.

2.3. Characterization

The specific surface area and pore size distribution of the biochars and magnetic biochars were analyzed by the Brunauer–Emmett–Teller (BET, BELSORP MaxII) N_2 adsorption/desorption method. The morphology before and after adsorption was analyzed by scanning electron microscopy (SEM, Tescan-MIRA LMS). The elemental compositions and surface properties were analyzed by energy dispersive spectroscopy (EDS, BRUKER XFlash 6130) and X-ray photoelectron spectroscopy (XPS, ThermoFisher Nexsa). The phase compositions of the biochars and magnetic biochars were determined by X-ray diffraction (XRD, Bruker D8 Advance). The structure and functional groups on the biochars and magnetic biochars were characterized using Fourier transform infrared spectroscopy (FTIR, IRTracer 100). The hysteresis return line and saturation magnetization intensity of the magnetic biochars was determined using a vibrating sample magnetometer (LakeShore 8604).

2.4. Adsorption Experiments

In order to achieve optimal utilization of raw materials, the optimal pyrolysis temperature of biochar needs to be determined before conducting batch adsorption experiments. This necessity arises from the fact that biochar produced at varying pyrolysis temperatures yields different amounts of carbon. Biochar was prepared at temperatures of 200, 300, 350, 400, 500, and 600 °C; the relevant formulas are as follows.

Simultaneously, the prepared biochar underwent ash content determination: a precisely weighed sample of 1 g was placed in a porcelain crucible and subjected to pyrolysis in a muffle furnace with an open mouth at a temperature of 800 °C for a duration of two hours. After cooling down to room temperature, the sample was reweighed. The ash content was calculated as the percentage change in mass before and after ashing; the relevant formulas are as follows:

$$carbon\ yield\ A = \frac{M_1}{M_0} \times 100\% \quad (1)$$

$$ash\ content\ B = \frac{N_1}{N_0} \times 100\% \quad (2)$$

where A is the biochar yield (%), M_0 is the mass of biomass (g), and M_1 is the mass of biochar (g). B is the biochar ash content (%), N_0 is the mass of biochar before ashing (g), and N_1 is the mass of ashing product (g).

A batch of adsorption experiments was carried out under different conditions to select the best removal performance of biochar and magnetic biochar on heavy metal Sb, including different aquatic plant species (Typha angustifolia, Eichhornia crassipes, and Arundo donax), biochar dosage (10–200 mg), pH (4–9), and ionic strength (0–0.05 mol/L NaOH). Specifically, the adsorption test was initiated by adding 30 mL of 5 mg/L Sb solution and a certain amount of the different biochars (or magnetic biochars) to a 100 mL reaction vial. Then, the mixture was agitated using a shaker with a shaking speed of 200 rpm at 25 °C for 12 h. A blank control group was included for each experiment, and three parallel groups were included to reduce errors. After reaching adsorption equilibrium, the mixture was centrifuged, and the concentration of Sb in the supernatant was detected to calculate the removal efficiency (R, %) and the amounts of Sb adsorbed at equilibrium (Q_e, mg/g). The distribution coefficient (K_d) represents the ratio of solid phase concentration to solution concentration of LMBC in the system when adsorption reaches equilibrium. The relevant formulas are as follows [19]:

$$removal\ efficiency\ R = \frac{100(C_0 - C_e)}{C_0} \quad (3)$$

$$the\ adsorption\ amount\ at\ equilibrium\ Q_e = \frac{100(C_0 - C_e)v}{m} \quad (4)$$

where C_0 and C_e are the initial concentration and equilibrium concentration of Sb (mg/L), respectively; m is the mass of the biochar and magnetic biochar (mg); and v is the solution volume (30 mL).

Additionally, adsorption kinetics [20] and isotherm experiments [21,22] were also conducted to explore the adsorption characteristics. Firstly, the optimum dosage of biochar and magnetic biochar was added to 150 mL of 5 mg/L Sb solution in a 250 mL Erlenmeyer flask, then shaken in an incubator shaker at 200 r/min at 25 °C for different time intervals. A blank control group was included for each experiment, and three parallel groups were included to reduce errors. After the experiment, the mixture was centrifuged, and the

concentration of Sb in the supernatant was detected to fit the appropriate kinetic model and isotherm model. The relevant formulas were as follows:

$$pseudo\text{-}first\text{-}order\ kinetic\ model\ Q_t = Q_e(1 - \exp(-k_1 t)) \quad (5)$$

$$pseudo\text{-}second\text{-}order\ kinetic\ model\ Q_t = \frac{k_2 {Q_e}^2 t}{k_2 Q_e t + 1} \quad (6)$$

$$Langmuir's\ isotherm\ model\ \frac{C_e}{Q_e} = \frac{C_e}{Q_m} + \frac{1}{Q_m K_L} \quad (7)$$

$$Freundlich's\ isotherm\ model\ \ln Q_e = \ln K_F + \frac{1}{n} \ln C_e \quad (8)$$

$$Separation\ factor\ R_L = \frac{1}{1 + K_L C_0} \quad (9)$$

where Q_t is the adsorption amount at time t (mg/g); Q_e is the adsorption amount at equilibrium (mg/g); k_1 is the pseudo-first-order rate constant (1/min); k_2 is pseudo-second-order rate constant (g/mg·min); Q_m is the maximum adsorption amount (mg/g); K_L is the Langmuir constant (L/mg); K_F is the Freundlich constant ((mg/g)/(mg/L)^n); n is an indicator of heterogeneity; R_L is the separation factor; and K_L is Langmuir's constant, L/mg.

2.5. Determination of Sb

An inductively coupled plasma mass spectrometer (ICP-MS, NexION 300X) was used to determine the concentration of Sb in the supernatant. The main instrument parameters were as follows: plasma RF power 1.1 kW, atomizer gas flow rate 1.1 L/min, auxiliary gas flow rate 0.8 L/min, cooling gas flow rate 14.0 L /min, sampling depth 5.0 mm, measurement method STD, scanning times 100, and residence time 10 ms [23].

2.6. Data Processing and Analysis Methods

All the data in this paper were processed and graphed using Microsoft Excel and Originlab Origin 2022 software. Analysis of variance (ANOVA) was applied to test the differences between treatments, and $p < 0.05$ was judged as statistically significant. All data are shown as the mean (and standard deviation) of three replicates.

3. Results and Discussion

3.1. Characterization of the Materials

BET The N_2 adsorption and desorption isothermal curves of the prepared LBC and LMBC are presented in Figure 2. It is evident that these results align with type IV isothermal curves and exhibit a type H4 hysteresis loop, indicating that both LBC and LMBC are primarily mesoporous and microporous materials, featuring some slit-like pores [24]. Table 1 shows that the specific surface area of LBC was 3.22 m^2/g, with an average pore size of 12.39 nm and a pore volume of 0.099 cm^3/g. It is worth noting that the specific surface area of LMBC was 89.14 m^2/g, with an average pore size of 7.97 nm and a pore volume of 0.18 cm^3/g, which represented a significant increase in the specific surface area and pore volume compared with that of LBC, indicating that LMBC might have greater adsorption potential than LBC. When the co-precipitation method is employed to prepare LMBC, NaOH is utilized for the aging reaction. The isothermal adsorption/desorption curve indicates that LMBC predominantly exhibits a mesoporous structure. It can be inferred that the alkalization process degrades the micropore walls, thereby reducing the specific surface area and volume of micropores while generating a significant quantity of mesoporous pores. Consequently, the mesoporous specific surface area increases, leading to an overall enhancement in the total specific surface area and pore volume of LMBC [25].

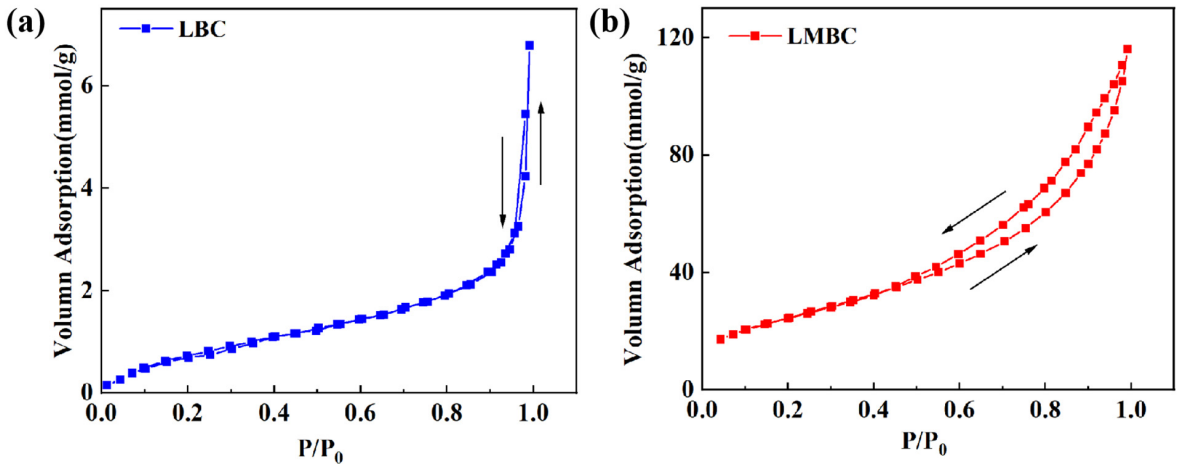


Figure 2. Adsorption and desorption isothermal curves of LBC (**a**) and LMBC (**b**).

Table 1. Specific surface area and pore structure of LBC and LMBC.

Biochar	BET Surface Area (m^2/g)	Total Pore Volume (cm^3/g)	Average Pore Diameter (nm)
LBC	3.22	0.099	12.39
LMBC	89.14	0.182	7.97

SEM Figure 3 illustrates the microtopography of LBC and LMBC before and after adsorption. As observed in Figure 3a,c, the surface of LBC was smooth and flat prior to adsorption, whereas the surface of LMBC exhibited collapse and cracks. This indicates that the magnetization modification generated a greater number of reaction sites on LMBC, which facilitated the adsorption process. Following the adsorption of Sb, as depicted in Figure 3b,d, numerous particulate matters appeared on the surfaces of both LBC and LMBC. These particulates are likely to be adsorbed substances, including Sb compounds.

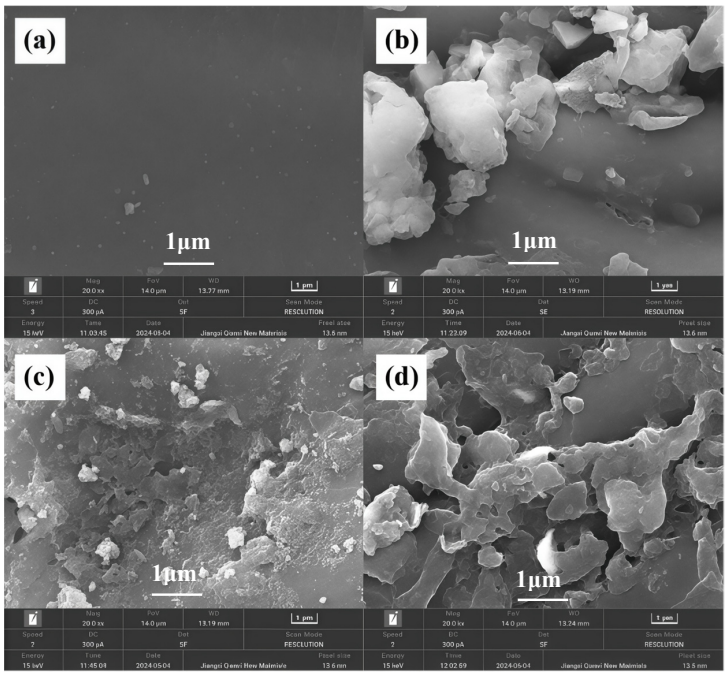


Figure 3. Scanning electron micrographs of LBC and LMBC before and after adsorption. (**a**) LBC-before adsorption; (**b**) LBC-after adsorption; (**c**) LMBC-before adsorption; (**d**) LMBC-after adsorption.

EDS The fluorescence diagrams and atomic number percentages are presented in Figure 4 and Table 2. It can be concluded that the primary element in LBC and LMBC is carbon (C), as its atomic number percentage exceeds 50%, followed by oxygen (O), nitrogen (N), and iron (Fe). Notably, the content of Fe in LMBC increased significantly to 7.88% compared to just 0.07% in LBC. Additionally, the fluorescence diagram indicates a marked increase in blue fluorescent dots corresponding to Fe, suggesting that iron was successfully incorporated onto the surface of LMBC during the magnetic modification process.

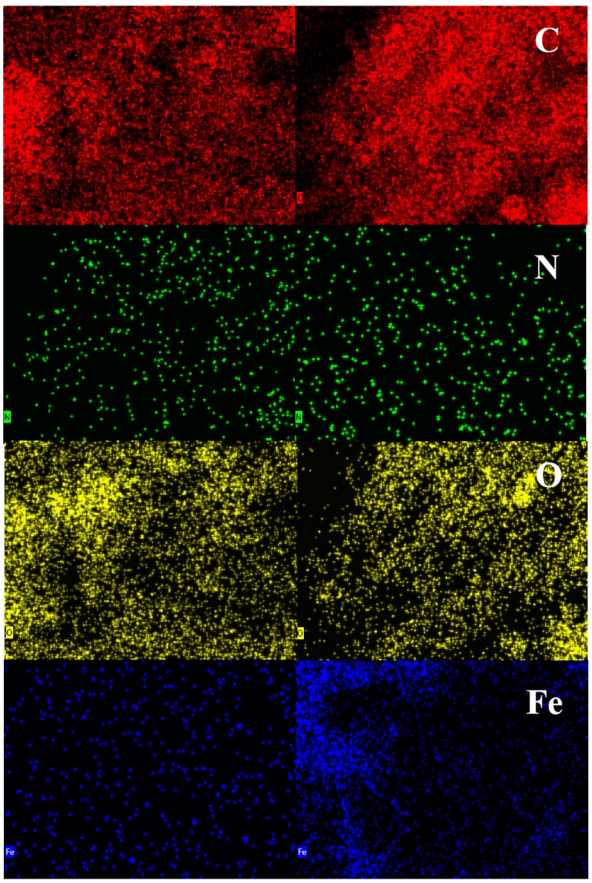


Figure 4. C, N, O, and Fe energy spectrum fluorescence of LBC and LMBC.

Table 2. The element contents of LBC and LMBC.

Element	Atomic Ratio (%)	
	LBC	LMBC
C	60.96	54.62
O	34.94	32.86
N	4.03	4.64
Fe	0.07	7.88

FTIR The results of functional group changes of LBC and LMBC before and after adsorption are presented in Figure 5. The infrared spectra before and after Sb adsorption are basically the same, indicating that the basic structure of the material has not changed. The peaks observed between 3000 and 3500 cm^{-1} correspond to the stretching vibrations of unsaturated C-H and O-H bonds [26]. Additionally, the peaks within the range of 1450–1650 cm^{-1} are attributed to the stretching vibrations of C=C bonds found in the aromatic hydrocarbon benzene ring skeleton [27]. Peaks located at 1010–1120 cm^{-1} correspond to C-O-C, which is a characteristic peak associated with glycosidic bonds present in polysac-

charides; notably, this peak shifted post-adsorption and exhibited reduced intensity [28]. The peaks at 1366 cm^{-1} and 1440 cm^{-1} were symmetric and antisymmetric vibrational bands attributed to the ionic carboxyl groups. It is evident that, after adsorption, these bands shifted collectively to 1441 cm^{-1}, suggesting that -COOH groups participated in the Sb adsorption process. This shift likely resulted from coordination interactions between Sb ions and oxygen-containing functional groups [29]. The FTIR spectra indicated that the main structure of LBC was aromatic hydrocarbon, which had many hydroxyl groups and other sites favorable for the adsorption of Sb. The formation of magnetite on the surface of LMBC was further confirmed by the observation of a strong characteristic peak of Fe-O vibration of magnetite at 580 cm^{-1} and the Fe-OH bond at 679 cm^{-1} [30].

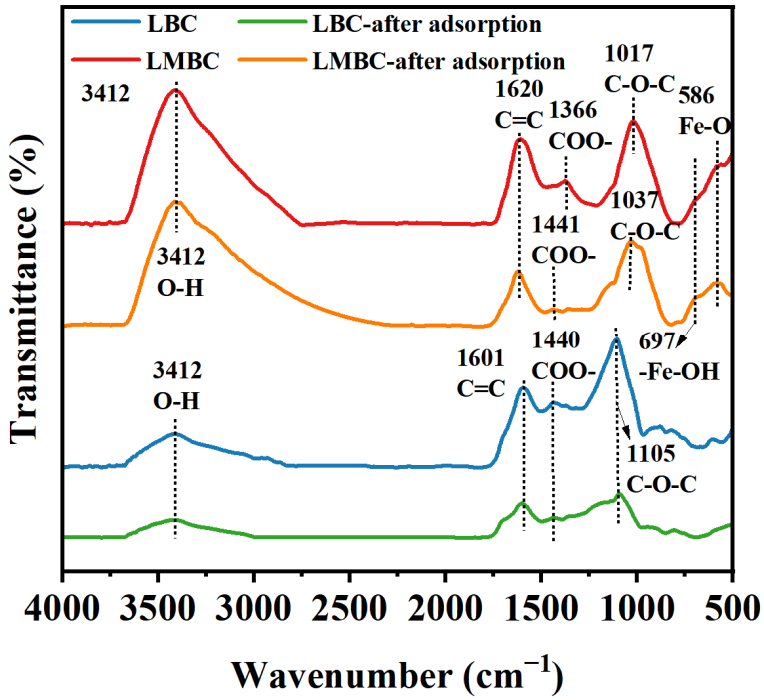


Figure 5. The FTlR results of LBC and LMBC before and after absorption.

XRD The XRD patterns of LBC and LMBC before and after adsorption are presented in Figure 6. It is evident that there were relatively obvious diffraction peaks in the LBC near 2θ = 21.31° before and after adsorption, which might be the presence of amorphous carbon. In the range of 2θ from 26.02° to 27.89°, there were obvious characteristic diffraction peaks in the spectrum of LBC, which might be caused by the pyrolytic carbonization of biomass at high temperatures, resulting in the precipitation of carbonates and the highlighting of $CaCO_3$ diffraction peaks [31]. The characteristic peaks appearing at 2θ of 30.17°, 35.59°, 43.15°, and 56.93° for LMBC and LMBC-Sb corresponded to the (220), (311), (400), and (511) crystal faces in the Fe_3O_4 cubic crystal, which is in accordance with JCPDS:26-1136 standard cards. The characteristic peaks at 2θ of 33.12°, 40.83°, and 54.04° corresponded to the (104), (113), and (116) crystal faces in Fe_2O_3 cubic crystals, which is in accordance with JCPDS: 72-0469 standard cards [32]. The characteristic peaks observed at 2θ angles of 31.22° and 38.54° were indicative of the formation of Sb_2O_3 and Sb_2O_5, respectively, within the LMBC framework during the adsorption process. The results suggested that the oxidized iron oxides present in LMBC interacted with Sb through a combination of adsorption and co-precipitation.

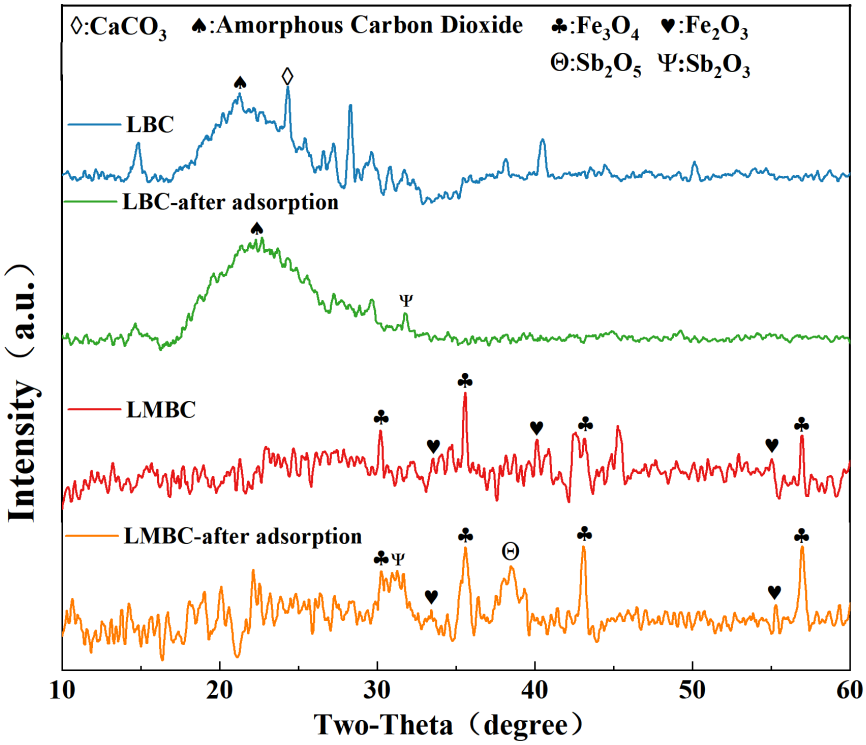


Figure 6. XRD pattern of LBC and LMBC before and after adsorption.

XPS The XPS spectra of LMBC before and after the adsorption revealed that C, O, and Fe were the main elements (Figure 7a), confirming the successful loading of Fe on the LMBC. Notably, new peaks corresponding to Sb appeared in the spectrum following adsorption, indicating that Sb was effectively adsorbed by LMBC. The observed decrease in the percentage of C-C bonds (Figure 7b) demonstrated that C-C bonds were broken as a result of the redox reaction [33]. Additionally, an increase in the percentage of Metal-O peaks (Figure 7c) confirmed that metal oxides formed post-adsorption as a result of Sb addition [34]. The Fe 2p region (Figure 7d) was deconvoluted into five peaks, with the peaks at 724.8 eV, 711.5 eV, and 710.3 eV assignable to Fe^{3+} and Fe^{2+} species, respectively [35]. Before adsorption, the masses of Fe^{3+} and Fe^{2+} were 74.19% and 20.54%, respectively. After adsorption, the percentage of Fe^{3+} decreased to 58.74%, while that of Fe^{2+} increased to 31.39%. This change suggests that some portion of Fe^{3+} acted as an oxidant during this process, providing substantial support for the proposed mechanism underlying Sb oxidation removal. Furthermore, these spectral peaks exhibited shifts towards lower binding energies upon complexation with Sb species; this observation implies that an inner-sphere complex was generated between iron-oxygen moieties and Sb species. The masses of Sb^{5+}, Fe-Sb, and Sb^{3+} species in the Sb peaks after adsorption were 67.32%, 28.76%, and 3.92%, respectively (Figure 7e), which proved that Sb had been adsorbed by LMBC and indicated that part of Sb^{3+} in LMBC was oxidized to Sb^{5+} [36].

Table 3 presents the elemental atomic ratio of LMBC before and after adsorption. It can be seen that, after adsorption of Sb, the O/C ratio of LMBC decreased from 0.9 to 0.69, which indicated that the oxygen-containing groups were reduced during the process, and the atomic ratio of Fe decreased from 16.64 to 9.13, while the atomic ratio of Sb increased from 0.04 to 15.97, indicating that LMBC effectively adsorbed Sb through a redox mechanism.

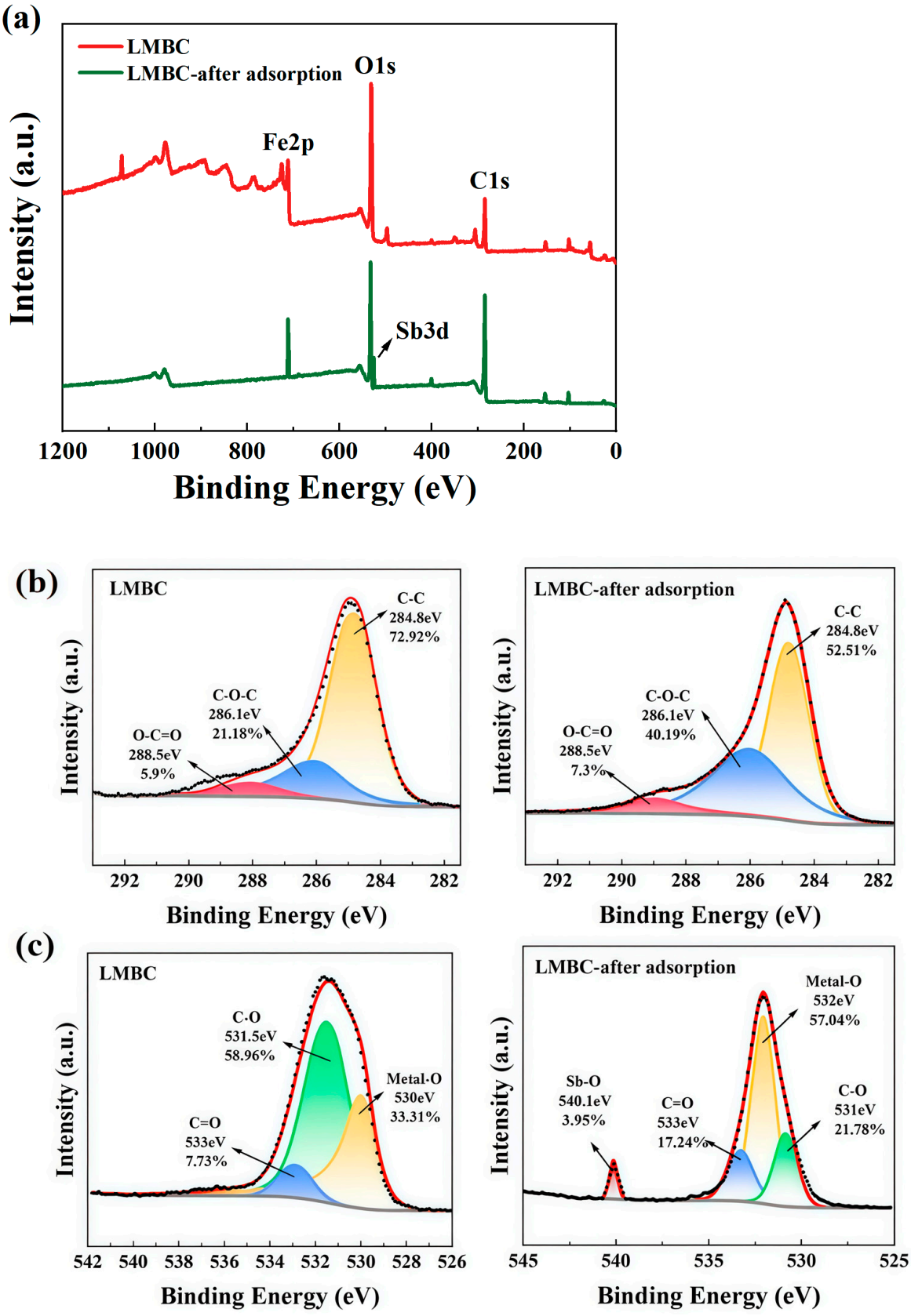


Figure 7. *Cont.*

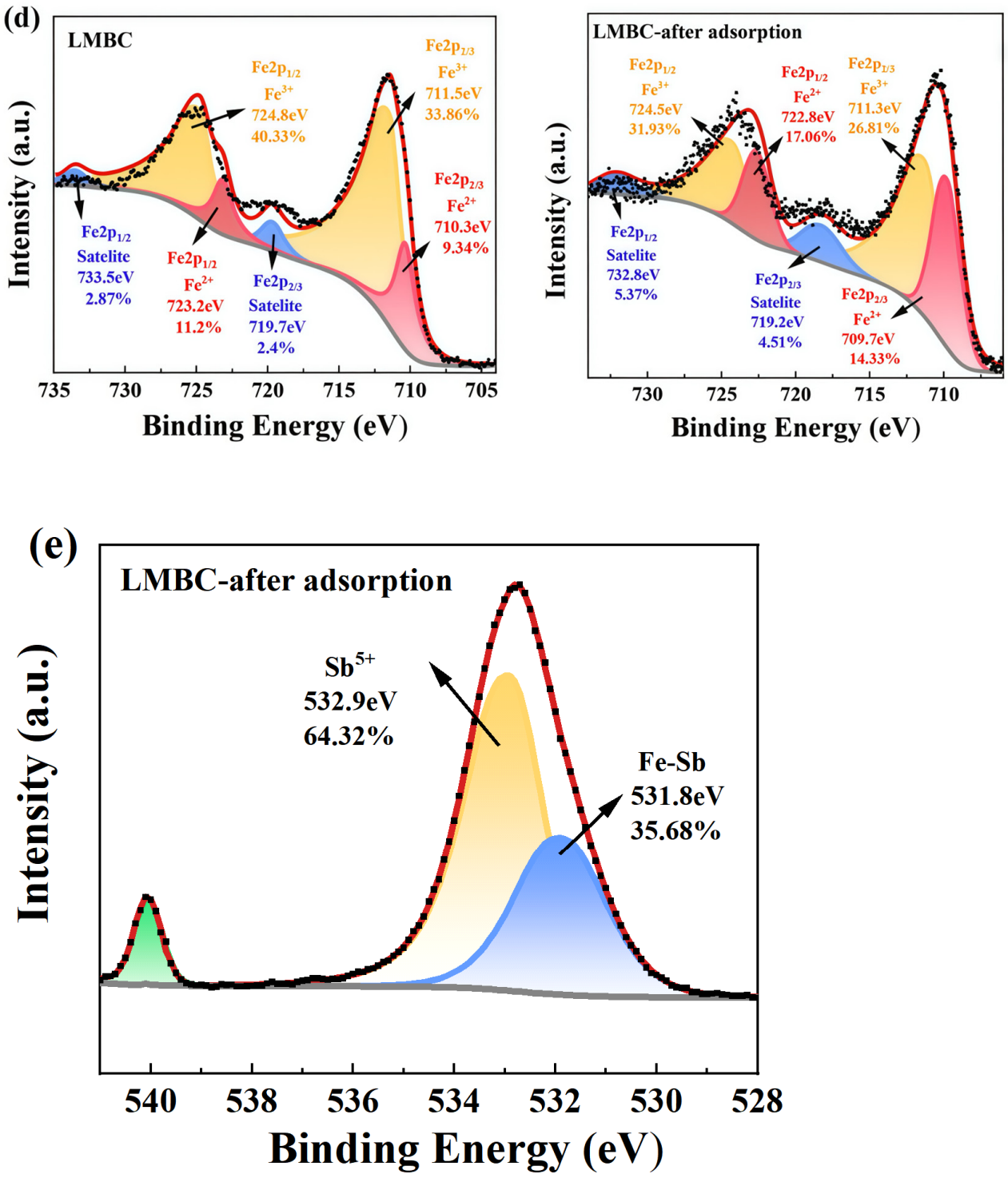


Figure 7. XPS spectra of LMBC before and after adsorption. (**a**) Full spectrum; (**b**) C1s fine spectrum; (**c**) O1s fine spectrum; (**d**) Fe2p fine spectrum; and (**e**) Sb3d fine spectrum.

Table 3. Elemental content of LMBC before and after adsorption.

Sample	Atomic Ratio (%)					
	C 1s	O 1s	Fe 2p	N 1s	Sb 3d	O/C
LMBC	42.13	38.14	16.64	2.85	0.04	0.9
LMBC-after adsorption	43.04	29.83	9.13	2.03	15.97	0.69

Magnetism Figure 8 shows the magnetization curve of LMBC, and it can be seen that its hysteresis curve converged with the non-hysteresis curve, which indicated that there was no remanence and coercivity, and also confirmed its superparamagnetism. As a result, LMBC is easy to collect, utilize, and recycle through magnetic fields [37].

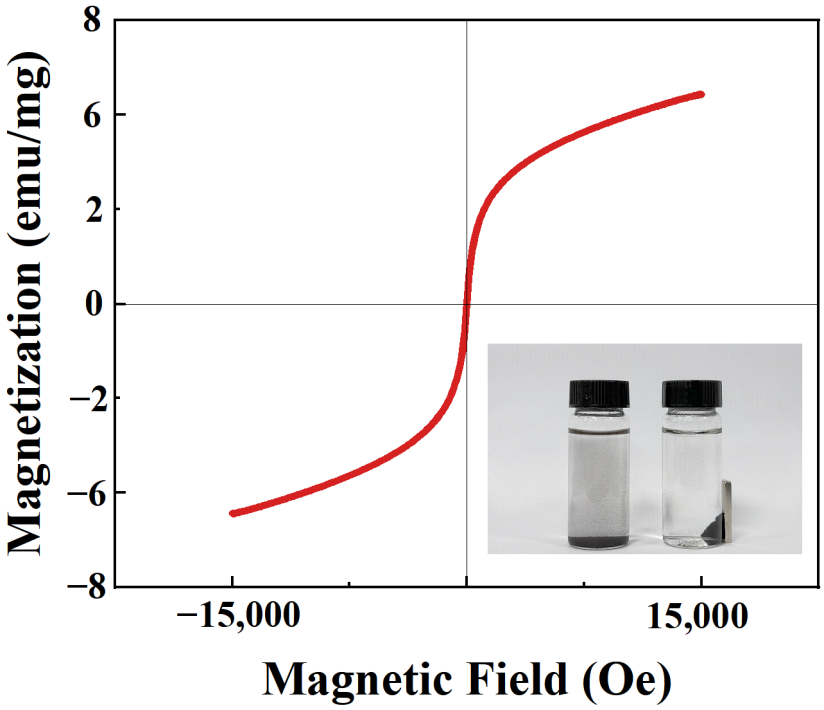


Figure 8. Magnetization curve of LMBC.

3.2. Effect of Different Influencing Factors on Sb Adsorption

(1) Effect of pyrolysis temperature

The experimental results of pyrolysis temperatures of the three aquatic plants showed the same trend; An example represented by Arundo donax is shown in the Tables 4 and 5.

Table 4. Char yield at different pyrolysis temperatures.

Biochar	Pre-Carbonization Quality/g	Post-Carbonization Quality/g	Yield/%
BC200	15.0082	N/A	N/A
BC300	15.0036	7.6125	50.73
BC350	15.0095	6.4117	42.75
BC400	15.0048	5.0468	33.63
BC500	15.0076	3.4215	22.80
BC600	15.0024	0.1586	1.06

N/A stands for "not available" and indicates that no meaningful data could be obtained from the experiment.

Table 5. Ash content at different pyrolysis temperatures.

Biochar	Mass Before Greying/g	Mass of Ashing Product/g	Ash Content/%
BC300	1.0018	0.2419	24.15
BC350	1.0004	0.2719	27.18
BC400	1.0007	0.3102	30.99
BC500	1.0012	0.3765	37.6
BC600	1.0003	0.6895	68.92

As illustrated in Table 4, optimizing the preparation temperature to achieve the highest char yield is crucial for maximizing the efficiency of biomass raw material utilization. At excessively low temperatures (<300 °C), the characteristics of the prepared biochar indicate that the biomass has not been sufficiently converted into char. Conversely, at excessively high temperatures (>500 °C), the biomass is nearly completely reduced to ash.

As a consequence of the increased loss of organic matter associated with elevated pyrolysis temperatures, the ash content of biochar tends to rise. A higher carbon content in biochar correlates with a reduced proportion of oxidized to inorganic ash, and vice versa. Table 5 demonstrates that the ash concentration in biochar progressively increases as the pyrolysis temperature is elevated; at 300 °C, the carbon content of biochar is relatively high. Therefore, 300 °C was chosen as the optimal pyrolysis temperature for producing biochar.

(2) Effects of different aquatic plant species

The adsorption capacity of biochar and magnetic biochar prepared by different aquatic plant species is illustrated in Figure 9a. It is evident that the adsorption capacity of the magnetic biochar for Sb was much higher than that of the unmodified biochar, and the adsorption effect was ranked as LMBC > XMBC> FMBC > LBC> FBC > XBC. As a result, LMBC had the highest adsorption rate of Sb, reaching up to 88.78%. As a result, biochar (LBC) and magnetic biochar (LMBC) produced from Arundo donax were selected as the optimal materials for further studies on adsorption.

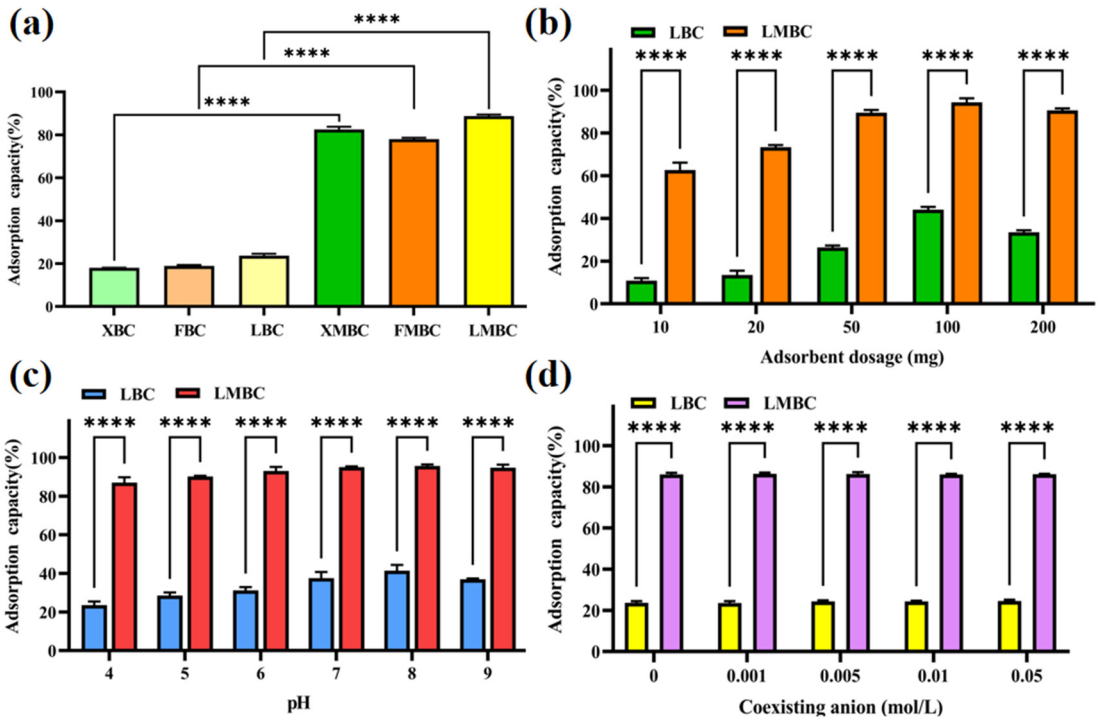


Figure 9. (**a**) Effect of biochar and magnetic biochar prepared by different aquatic plant species; (**b**) effect of biochar and magnetic biochar dosage; (**c**) effect of initial pH; and (**d**) effect of ionic strength. "****": the number of asterisks denotes the level of statistical significance, with four asterisks indicating a *p*-value of less than 0.0001, signifying a highly significant difference between LBC and LMBC.

(3) Effect of dosage of biochar

The adsorption capacity of different dosages of LBC and LMBC is illustrated in Figure 9b. It is evident that the adsorption capacity of LMBC consistently exceeded that of LBC at equivalent dosage levels. As the dosage of LMBC increased from 10 mg to 100 mg,

the adsorption capacity for Sb significantly rose from 60.14% to 92.93%. However, when the dosage of LMBC was higher than 100 mg, the adsorption capacity of Sb slightly decreased, which might be attributed to the decreased number of sites and active groups per unit mass of LMBC. Previous studies have indicated that a specific quantity of sites and active groups on biochar surfaces can enhance Sb adsorption; however, an excessive abundance may lead to competition among Sb ions in solution for these sites, ultimately diminishing overall adsorption efficiency [38]. Therefore, 100 mg of biochar was chosen as the optimal dosage level.

(4) Effect of pH

It has been established that the solution pH has a significant impact on the protonation and deprotonation of functional groups on the adsorbent surface, affecting target ion adsorption [39]. As illustrated in Figure 9c, the adsorption rate of LMBC for Sb was 88.48% at a pH of 4. With an increase in pH, this rate reached a maximum of 96.64% at a pH of 8; however, it slightly decreased when the pH rose to 9. Because the standard solution of Sb used in the experiment is a mixed solution, in the pH range of 4 to 9, Sb(V) mainly exists in the form of $Sb(OH)^{6-}$, and Sb(III) mainly exists in the form of $Sb(OH)_3$. With the increase in pH of the solution, the metal hydroxyl group (M-OH) on the surface of the material increases, which is conducive to complexation with $Sb(OH)_3$ [40]. However, with the increase of pH, deprotonation will occur on the surface of biochar, resulting in a large number of negatively charged functional groups, which is not conducive to the adsorption of $Sb(OH)^{6-}$ [41]. Based on these experimental findings, it can be concluded that a pH value of 8 represents the optimal condition for LMBC adsorption.

(5) Effect of ionic strength

The addition of specific ions such as Na^+, Cl^-, and $SO_4{}^{2-}$ can change the adsorption environment, thereby affecting the efficiency of adsorption. Consequently, the impact of ionic strength was investigated using NaCl as an interfering ion [42]. The results of different ionic strength during LBC and LMBC adsorption of Sb are shown in Figure 9d. It is evident that the adsorption capacity of LMBC for Sb remained at 86%, suggesting that ionic strength may have a minimal influence on Sb adsorption by LMBC.

Combined with the above analysis, it can be concluded that the optimal adsorption conditions of LMBC for Sb are 5 mg/L Sb solution with 100 mg LMBC at the initial pH of 8.

3.3. Adsorption Kinetics

Adsorption kinetics refers to the diffusion of chemicals within the adsorbed phase on the surface of adsorbent, which determines the time of interaction between the adsorbed substances and the solid–liquid interface [43].

The results of adsorption kinetics of LBC and LMBC are shown in Table 6 and Figure 10. As illustrated in Figure 10a,b, the adsorption kinetics of Sb by both LBC and LMBC can be generally categorized into three distinct stages: (1) the first stage is the fast adsorption of Sb in the initial 4 h; (2) the second stage is the gradual increase from 4 to 12 h; (3) the third stage is adsorption equilibrium from 12 to 24 h. LBC was more in line with the quasi-first-order kinetic model (R^2 = 0.995), indicating that the adsorption process was physisorption, and the actual equilibrium concentration of 4.23 mg/g was very close to the simulated equilibrium concentration of 4.47 mg/g. LMBC was more in line with the quasi-second-order kinetic model (R^2 = 0.999), indicating that the adsorption process was chemisorption, and the actual equilibrium concentration of 14.47 mg/g was very close to the simulated equilibrium concentration of 14.83 mg/g. In general, it can be concluded that the adsorption efficiency of LMBC was significantly stronger than that of LBC.

Table 6. The parameters of adsorption kinetics.

Materials	Quasi-First-Order Kinetic Model			Quasi Second-Order Kinetic Model		
	Q_e	k_1	R^2	Q_e	k_2	R^2
LBC	4.47	0.11	0.995	5.85	0.016	0.988
LMBC	14.99	0.252	0.942	14.83	0.035	0.999

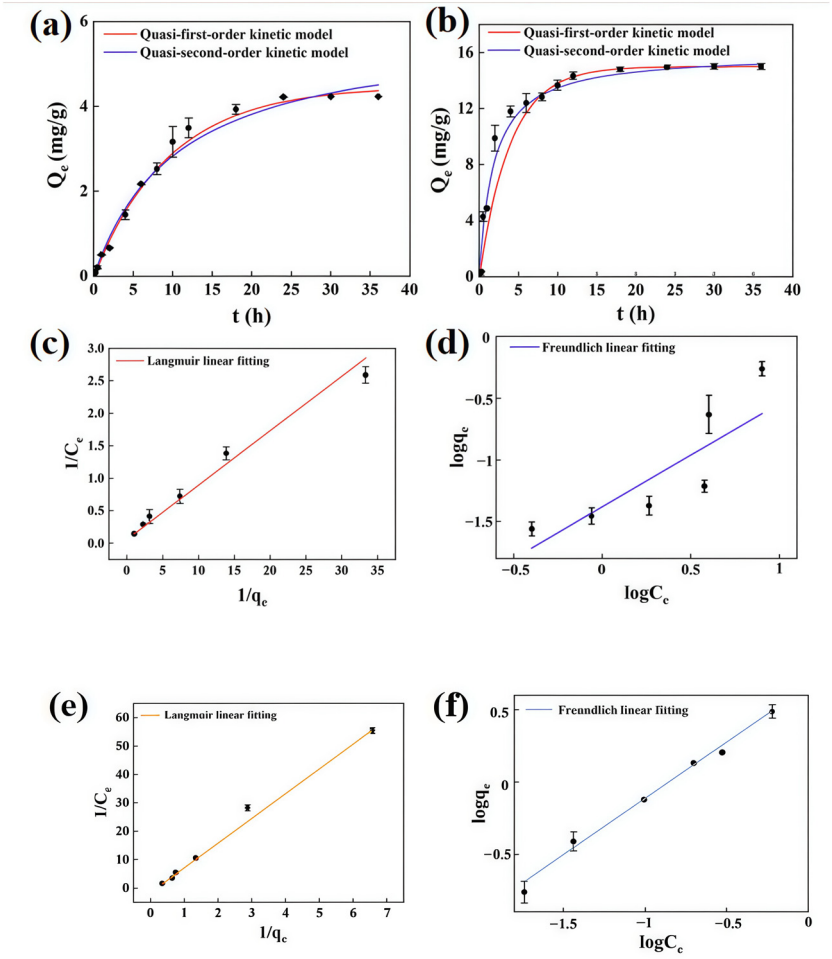


Figure 10. (**a**) Adsorption kinetics of LBC; (**b**) adsorption kinetics of LMBC; (**c**,**d**) adsorption isotherm of LBC; and (**e**,**f**) adsorption isotherm of LMBC (experimental conditions: 150 mL of 5 mg/L Sb solution with 100 mg LMBC at the initial pH of 8).

3.4. Adsorption Isotherm

Adsorption isotherm is widely utilized to characterize the distribution of adsorbates on adsorbents once the adsorption process has reached equilibrium [44]. The Langmuir model is the preferred equation for describing monomolecular layer adsorption at surface sites of the adsorbent, while the Freundlich model serves as an empirical equation frequently applied to multilayer heterogeneous adsorption.

As presented in Table 7, the adsorption isotherm of LBC was more in line with the Langmuir model (R^2 = 0.988), and LMBC was well fitted to both the Langmuir model and the Freundlich model, with a correlation coefficient R^2 of 0.999, indicating that the adsorption of LMBC was a simultaneous process of monolayer and multilayer adsorption, while that of LNC was mainly monolayer adsorption. The maximum adsorption capacities (Q_m) of LBC and LMBC were 7.89 mg/g and 26.07 mg/g, respectively. The suitability of the adsorbent for metal ion adsorption is indicated by the range of R_L constants, and calculations revealed that the R_L constants of LBC lie between 0.05 and 0.5, suggesting

good adsorption performance when $0 < R_L < 1$. This also indicated that the $1/n$ value of the Freundlich model was fitted to the model and the adsorption of LMBC. The K_L value of the Langmuir model for LMBC and the $1/n$ value of the Freundlich model were both between 0 and 1, signifying that the adsorption process occurs readily.

Table 7. The parameters of adsorption isotherm.

Materials	Langmuir Isothermal Adsorption Model				Freundlich Isothermal Adsorption Model		
	Q_m	K_L	R^2	R_L	$1/n$	K_F	R^2
LBC	7.89	1.73	0.988	0.103	0.065	0.047	0.736
LMBC	26.07	0.0044	0.999	0.978	0.813	4.5637	0.999

3.5. Potential Mechanisms

The potential mechanisms of the adsorption of Sb by LMBC may involve three distinct processes, which is succinctly demonstrated in Figure 11. Firstly, the porous structure of LMBC provides a vast array of adsorption sites, facilitating the immobilization of Sb ions that infiltrate its interior. Secondly, complexation reactions are critical; an increased presence of acidic oxygen-containing functional groups such as hydroxyl (-OH) and carboxyl (-COOH) enhances the formation of ionic bonds with metal ions [45], thereby enhancing adsorption capacity. Additionally, these functional groups, particularly the Fe-O moieties, reacted with Sb to form Fe-Sb complexes, which effectively anchor heavy metal ions to the biochar surface. Thirdly, the valence states interchanged between Fe^{2+} and Fe^{3+}, which were immobilized on the biochar surface through interactions with functional groups, constituting a pivotal mechanism in the adsorption process. Upon contact with Sb^{3+} and Sb^{5+}, these iron ions were displaced, thereby facilitating the sequestration of heavy metal ions. Concurrently, a redox reaction occurred during this ion-exchange process, where a portion of Sb^{3+} was oxidized to Sb^{5+}. This redox reaction was accompanied by a decrease in Fe^{3+} and a corresponding increase in Fe^{2+} concentration.

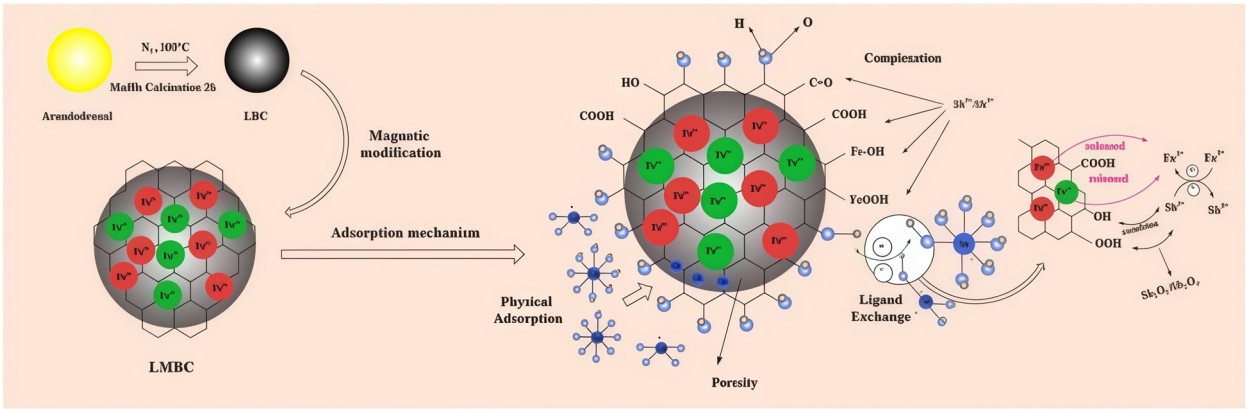


Figure 11. Schematic diagram of the mechanism of Sb adsorption and removal by LMBC.

However, the potential mechanisms of the adsorption of Sb by LBC might be relatively simple, which is mainly a physical adsorption process. Biochar itself has the characteristics of large pores, enabling immobilization of Sb ions that penetrated its interior. Although it also has acidic oxygen-containing functional groups such as hydroxyl (-OH) and carboxyl (-COOH), its strength and content were not as good as that of magnetic biochar. Moreover, the adsorption of Sb by LBC is only a single molecular layer adsorption, and its adsorption effect is far worse than that of LMBC.

3.6. Comparison of Other Reported Materials for the Removal of the Heavy Metal Sb with LMBC

Table 8 summarizes the various methods of synthesis of adsorbents for Sb in various forms, as well as their maximum adsorption amounts and the removal rate of Sb. In the treatment of Sb, most studies have selected raw materials such as iron powder and polyferric sulfate. While these materials are effective in addressing antimony pollution, they also have negative impacts on water quality. The use of aquatic plants as raw materials aligns with the principles of green environmental protection. Furthermore, it has been reported that higher initial concentrations of Sb, larger dosages of adsorbents, and extended adsorption durations can significantly enhance adsorption capacity [46]. Therefore, most of the adsorbents shown in the Table 8 were used in acidic (pH < 5) and alkaline (pH > 9) environments, and the highest initial Sb concentration of the adsorption experiments was >100 mg/L; consequently, the maximum adsorption amounts and removal rate of Sb of these materials could be higher. In fact, the initial Sb concentration in these studies is significantly higher than the contamination concentration of natural water and does not meet the environmental requirements for practical applications. In the present research, the initial Sb concentration used was at a low concentration of 0.5~10 mg/L, and the pH was close to that of natural water, which is more suitable to explore Sb pollution control in the actual environment. In general, the adsorption rate of LMBC for Sb can reach 97%, which makes it an excellent and efficient Sb adsorption material.

Table 8. Adsorption performance of Sb by different adsorbents.

Adsorbents	Modification Methods	pH	Equilibrium Time	Valence State of Sb	C_0 (mg/L)	Q_m (mg/g)	Dosage (g/L)	Removal Rate/%	Ref.
Graphene	N/A	11	4 h	Sb(III)	1~10	7.46	0.4	N/A	[47]
Birnessite and ferrihydrite	N/A	5	12 h	Sb(V)	0.12~24.35	17.6	0.5	93.3	[48]
Iron powder	Ball-milling and acid modification	5	6 h	Sb(V)	0~20	10.5	0.5	N/A	[49]
Microcystis aeruginosa microspheres	Loaded with magnetic nano-Fe_3O_4	4	2 h	Sb(III)	5~200	13.45	8.5	83.62	[50]
Fe-Mn LDH	Fe-Mn modification	5	150 min	Sb(III)	10	77.39	0.4	83.03	[51]
Fe_3O_4/TA/UiO-66	Nano-composite	3	24 h	Sb(III)	0.5~40	45	0.2	N/A	[52]
Fe-Zr binary oxide adsorbent	Co-precipitation method	7	3 h	Sb(V)	10	51	0.2	N/A	[53]
Fe-Zr binary oxide adsorbent	Co-precipitation method	7	3 h	Sb(V)	0.2	N/A	0.3	81	[54]
LaxFe-BC	Co-precipitation method	2	5 h	Sb(V)	10~100	18.92	1	N/A	[55]
Present research	Co-precipitation method	8	24 h	Sb	0.5~10	26.7	3	97	/

N/A indicates that the section was not addressed in the literature and the information was not available.

4. Conclusions

The present research utilized aquatic plants, including Arundo donax, Typha angustifolia, and Eichhornia crassipes, as raw materials to prepare biochar and magnetic biochar

for the adsorption and removal of Sb. Through experiments involving different influencing factors like aquatic plant species, biochar dosage, pH, and ionic strength, it was determined that LMBC had the highest removal rate of 97% of Sb under the best adsorption conditions of 5 mg/L Sb solution with 100 mg LMBC at an initial pH of 8. The quasi-second-order kinetic model and the Freundlich model have good correlation coefficients for the adsorption process of LMBC of Sb ($R^2 > 0.99$), indicating that the adsorption of Sb by LMBC is primarily physicochemical adsorption based on multilayer adsorption. Analysis by BET, SEM, EDS, FTIR, XRD, XPS, and VSM revealed that LMBC had good paramagnetism and a large surface area, and that Fe^{2+} and Fe^{3+} were successfully loaded by the method of magnetic modification during the co-precipitation process. Abundant hydroxyl groups and carboxyl groups were formed on the surface of LMBC, which played a dominant role in the adsorption enhancement. The possible adsorption mechanisms of Sb on LMBC include physical adsorption, ion exchange, surface complexation, and redox reaction, in which the formation of the Fe-Sb complex plays a major role in the adsorption of Sb. Consequently, LMBC is anticipated to be a special material for effectively removing antimony from water during the treatment of sudden water pollution incidents in natural water bodies.

Author Contributions: Investigation, L.N., Y.Z. (Yuxuan Zhu), and X.Z.; resources, L.Z.; writing—original draft, L.N.; writing—review and editing, Y.Z. (Yuting Zhang) and M.L.; funding acquisition, L.Z. All authors have read and agreed to the published version of the manuscript.

Funding: This work was supported by the National Key Research and Development program of China (No. 2023YFC3208702, 2022YFC3204001), and Central Public-Interest Scientific Institution Basal Research Fund (No. CKSF2024304+SH, CSF2023337/SH).

Data Availability Statement: Data are contained within the article.

Conflicts of Interest: The authors declare no conflict of interest.

References

1. He, M.; Wang, N.; Long, X.; Zhang, C.; Ma, C.; Zhong, Q.; Wang, A.; Wang, Y.; Pervaiz, A.; Shan, J. Antimony Speciation in the Environment: Recent Advances in Understanding the Biogeochemical Processes and Ecological Effects. *J. Environ. Sci.* **2019**, *75*, 14–39. [CrossRef] [PubMed]
2. Zhu, J.; Wu, F.C.; Deng, Q.J.; Shao, S.X.; Mo, C.L.; Pan, X.L.; Li, W.; Zhang, R.Y. Environmental characteristics of water near the Xikuangshan antimony mine, Hunan Province. *Acta Sci. Circumstantiae* **2009**, *29*, 655–661.
3. Li, X.H. Ecological Risk Assessment on Sediments in Sb-Mining Area and Development of Restoration Technology. Ph.D. Dissertation, Beijing Forestry University, Beijing, China, 2013.
4. Cidu, R.; Biddau, R.; Dore, E.; Vacca, A.; Marini, L. Antimony in the Soil–Water–Plant System at the Su Suergiu Abandoned Mine (Sardinia, Italy): Strategies to Mitigate Contamination. *Sci. Total Environ.* **2014**, *497–498*, 319–331. [CrossRef] [PubMed]
5. Ritchie, V.J.; Ilgen, A.G.; Mueller, S.H.; Trainor, T.P.; Goldfarb, R.J. Mobility and Chemical Fate of Antimony and Arsenic in Historic Mining Environments of the Kantishna Hills District, Denali National Park and Preserve, Alaska. *Chem. Geol.* **2013**, *335*, 172–188. [CrossRef]
6. Casiot, C.; Ujevic, M.; Munoz, M.; Seidel, J.L.; Elbaz-Poulichet, F. Antimony and arsenic mobility in a creek draining an antimony mine abandoned 85 years ago (upper Orb basin, France). *Appl. Geochem.* **2006**, *22*, 788–798. [CrossRef]
7. Yao, S.; Zhu, X.; Wang, Y.; Zhang, D.; Wang, S.; Jia, Y. Simultaneous oxidation and removal of Sb(III) from water by using synthesized CTAB/$MnFe_2O_4$/ MnO_2 composite. *Chemosphere* **2020**, *245*, 125601. [CrossRef] [PubMed]
8. Singh, J.; Jadeja, R. Recent Advances in Agricultural Waste Derived Magnetic Biochar for Removal of Heavy Metal Ions: Mechanistic Insights and Technological Innovation. *J. Mol. Struct.* **2025**, *1325*, 141005. [CrossRef]
9. Chen, W.; Meng, J.; Han, X.; Lan, Y.; Zhang, W. Past, Present, and Future of Biochar. *Biochar* **2019**, *1*, 75–87. [CrossRef]
10. Xiang, L.; Liu, S.; Ye, S.; Yang, H.; Song, B.; Qin, F.; Shen, M.; Tan, C.; Zeng, G.; Tan, X. Potential Hazards of Biochar: The Negative Environmental Impacts of Biochar Applications. *J. Hazard. Mater.* **2021**, *420*, 126611. [CrossRef] [PubMed]
11. Yin, Z.; Ping, Z.; Sikun, L.; Lihui, K.; Ting, K.; Junhan, C.; Yuanling, G.; Hong, Z. Research Progress of Magnetic Biochar Materials. *Mod. Chem. Res.* **2018**, *11*, 4–6.
12. Sun, M.; Wang, C.; Luo, Z.; Zhu, X. Synthesis of Magnetic Biochar with High Iron Content and Large Specific Surface Area: Synergistic Effect of Fe Doping and KOH Activation. *J. Anal. Appl. Pyrolysis* **2023**, *173*, 106096. [CrossRef]

13. Chen, G.; Zhu, H.; Chen, H.; Guo, Y.; Xian, Q. Adsorption of microcystin-LR by Mg-modified aquatic plantbiochar in water. *Environ. Chem.* **2024**, *43*, 250–263.
14. Bayuo, J.; Rwiza, M.J.; Choi, J.W.; Njau, K.N.; Mtei, K.M. Recent and Sustainable Advances in Phytoremediation of Heavy Metals from Wastewater Using Aquatic Plant Species: Green Approach. *J. Environ. Manag.* **2024**, *370*, 122523. [CrossRef] [PubMed]
15. Lin, X.; Mou, R.; Cao, Z.; Xu, P.; Wu, X.; Zhu, Z.; Chen, M. Characterization of Cadmium-Resistant Bacteria and Their Potential for Reducing Accumulation of Cadmium in Rice Grains. *Sci. Total Environ.* **2016**, *569–570*, 97–104. [CrossRef]
16. Fritioff, A.; Greger, M. Uptake and distribution of Zn, Cu, Cd, and Pb in an aquatic plant *Potamogeton natans*. *Chemosphere* **2006**, *63*, 220–227. [CrossRef]
17. Zhang, J.; Li, Y.; Zhang, C.; Jing, Y. Adsorption of malachite green from aqueous solution onto carbon prepared from Arundo donax root. *J. Hazard. Mater.* **2008**, *150*, 774–782. [CrossRef]
18. Saarela, T.; Lafdani, E.K.; Laurén, A.; Pumpanen, J.; Palviainen, M. Biochar as Adsorbent in Purification of Clear-Cut Forest Runoff Water: Adsorption Rate and Adsorption Capacity. *Biochar* **2020**, *2*, 227–237. [CrossRef]
19. Revellame, E.D.; Fortela, D.L.; Sharp, W.; Hernandez, R.; Zappi, M.E. Adsorption Kinetic Modeling Using Pseudo-First Order and Pseudo-Second Order Rate Laws: A Review. *Clean. Eng. Technol.* **2020**, *1*, 100032. [CrossRef]
20. Pehlivan, E.; Cetin, S. Sorption of Cr(VI) Ions on Two Lewatit-Anion Exchange Resins and Their Quantitative Determination Using UV–Visible Spectrophotometer. *J. Hazard. Mater.* **2009**, *163*, 448–453. [CrossRef] [PubMed]
21. Xu, W.; Wang, H.; Liu, R.; Zhao, X.; Qu, J. The Mechanism of Antimony(III) Removal and Its Reactions on the Surfaces of Fe–Mn Binary Oxide. *J. Colloid Interface Sci.* **2011**, *363*, 320–326. [CrossRef] [PubMed]
22. Pan, Y.; Li, H.; Zhang, X.-X.; Zhang, Z.; Tong, X.-S.; Jia, C.-Z.; Liu, B.; Sun, C.-Y.; Yang, L.-Y.; Chen, G.-J. Large-Scale Synthesis of ZIF-67 and Highly Efficient Carbon Capture Using a ZIF-67/Glycol-2-Methylimidazole Slurry. *Chem. Eng. Sci.* **2015**, *137*, 504–514. [CrossRef]
23. Wen, Z.; Zenghui, H.; Jin, L.; Xiandeng, H.; Xiaoming, J. Highly Sensitive Determination of Trace Antimony in Water Samples by Cobalt Ion Enhanced Photochemical Vapor Generation Coupled with Atomic Fluorescence Spectrometry or ICP-MS. *Anal. Chim. Acta* **2022**, *1191*, 339361.
24. Groen, J.C.; Peffer, L.A.A.; Pérez-Ramírez, J. Pore Size Determination in Modified Micro- and Mesoporous Materials. Pitfalls and Limitations in Gas Adsorption Data Analysis. *Microporous Mesoporous Mater.* **2003**, *60*, 1–17. [CrossRef]
25. Xie, H.; Liu, C.; Shen, J.; Huang, N.; Xu, J. Preparation of ZSM-5 with hierarchical pores by Alkali treatment and Fe-modified and its catalytic performance for synthesis of diphenylmethane. *Pet. Process. Petrochem.* **2024**, *55*, 47–53.
26. Aljeboree, A.M.; Alshirifi, A.N.; Alkaim, A.F. Kinetics and Equilibrium Study for the Adsorption of Textile Dyes on Coconut Shell Activated Carbon. *Arab. J. Chem.* **2017**, *10*, S3381–S3393. [CrossRef]
27. Liu, S.; Li, J.; Xu, S.; Wang, M.; Zhang, Y.; Xue, X. A Modified Method for Enhancing Adsorption Capability of Banana Pseudostem Biochar towards Methylene Blue at Low Temperature. *Bioresour. Technol.* **2019**, *282*, 48–55. [CrossRef] [PubMed]
28. de Araújo, T.P.; Quesada, H.B.; dos Santos, D.F.; da Silva Fonseca, B.C.; Barbieri, J.Z.; Bergamasco, R.; de Barros, M.A.S.D. Acetaminophen Removal by Calcium Alginate/Activated Hydrochar Composite Beads: Batch and Fixed-Bed Studies. *Int. J. Biol. Macromol.* **2022**, *203*, 553–562. [CrossRef] [PubMed]
29. He, Y.; Sun, R.; Zhang, D.; Wang, Y.; Zhou, S.; Deng, X.; Wang, B.; Hu, G. Separable Alginate Gel Spheres Encapsulated with La-Fe Modified Biochar for Efficient Adsorption of Sb(III) with High Capacity. *J. Hazard. Mater.* **2023**, *460*, 132322. [CrossRef] [PubMed]
30. Shahmoradi, B.; Wantala, K.; Jari, H.; Zandsalimi, Y.; Mohammadloo, S.; Maleki, A.; Shivaraju, H.P.; Choi, S.-S.; Lee, S.-M. Removal of Humic Acid from Aqueous Media Using Magnetite Nanoparticles. *Desalination Water Treat.* **2021**, *210*, 273–280. [CrossRef]
31. Ding, L.; Wei, Y.; Wang, Y.; Chen, H.; Caro, J.; Wang, H. A Two-Dimensional Lamellar Membrane: MXene Nanosheet Stacks. *Angew. Chem. Int. Ed.* **2017**, *56*, 1825–1829. [CrossRef]
32. Zhang, M.; Cushing, B.L.; O'Connor, C.J. Synthesis and Characterization of Monodisperse Ultra-Thin Silica-Coated Magnetic Nanoparticles. *Nat. Nanotechnol.* **2008**, *19*, 085601. [CrossRef] [PubMed]
33. Zhang, S.; Cao, Y.; Gao, C.; Meng, T.; Li, Q.; Jiang, D. Removal of Sb(III) and Sb(V) from water by sulfur-iron modified biochar. *Mod. Chem. Ind.* **2024**, *44*, 1–11.
34. Smith, M.; Scudiero, L.; Espinal, J.; McEwen, J.-S.; Garcia-Perez, M. Improving the Deconvolution and Interpretation of XPS Spectra from Chars by *Ab Initio* Calculations. *Carbon* **2016**, *110*, 155–171. [CrossRef]
35. Yamashita, T.; Hayes, P. Analysis of XPS Spectra of Fe^{2+} and Fe^{3+} Ions in Oxide Materials. *Appl. Surf. Sci.* **2008**, *254*, 2441–2449. [CrossRef]
36. Stamenković, T.; Bundaleski, N.; Barudžija, T.; Validžić, I.; Lojpur, V. XPS Study of Iodine and Tin Doped Sb_2S_3 Nanostructures Affected by Non-Uniform Charging. *Appl. Surf. Sci.* **2021**, *567*, 150822. [CrossRef]
37. Dube, D.; Parekh, C.; Nyoni, B. Removal of Chromium and Nickel from Electroplating Wastewater Using Magnetite Particulate Adsorbent: (1) Effect of pH, Contact Time and Dosage, (2) Adsorption Isotherms and Kinetics. *Mod. Appl. Sci.* **2016**, *10*, 222–232. [CrossRef]

38. Liao, L.; Wu, P.; Wang, B.; Li, L.; Han, Z. Removal of Sb(V) from Antimony-Rich Wastewater by Modified Biochar. *Chin. J. Environ. Eng.* **2021**, *15*, 435–445.
39. Wang, X.; Wang, T.; Song, C.; Zhang, Y.; Yang, K.; Wang, J.; Xu, X.; He, F. Competitive Adsorption Behavior of As(V) and Sb(V) on Hematite: Facet and pH Dependent Coordination Affinity and Role of Outer-Sphere Complexes. *Sep. Purif. Technol.* **2025**, *354*, 128916. [CrossRef]
40. Cheng, Q.; Li, Q.; Huang, X.; Li, X.; Wang, Y.; Liu, W.; Lin, Z. The High Efficient Sb(III) Removal by Cauliflower like Amorphous Nanoscale Zero-Valent Iron (a-nZVI). *J. Hazard. Mater.* **2022**, *436*, 129056. [CrossRef] [PubMed]
41. Peng, L.; Li, H.; Lin, W.; Xiao, T.; Wang, J.; Tang, J.; Wang, N. Sorption of Antimony(V) to Naturally Formed Multicomponent Secondary Iron Minerals: Sorption Behavior and a Comparison with Synthetic Analogs. *Sci. Total Environ.* **2024**, *907*, 168125. [CrossRef]
42. Ye, Z.; Xu, D.; Zhong, J.; Gao, S.; Wang, J.; Zhang, Y.; Xu, H.; Li, Y.; Li, W. Influence of Soil Colloids on the Transport of Cd^{2+} and Pb^{2+} under Different pH and Ionic Strength Conditions. *Agronomy* **2024**, *14*, 352. [CrossRef]
43. Nizam, T.; Krishnan, K.A.; Joseph, A.; Krishnan, R.R. Isotherm, Kinetic and Thermodynamic Modelling of Liquid Phase Adsorption of the Heavy Metal Ions Zn(II), Pb(II) and Cr(VI) onto $MgFe_2O_4$ Nanoparticles. *Groundw. Sustain. Dev.* **2024**, *25*, 101120. [CrossRef]
44. Takeda, N.; Fukushi, K.; Okuyama, A.; Takahashi, Y. Solid-Liquid Partitioning and Speciation of Pb(II) and Cd(II) on Goethite under High pH Conditions, as Examined by Subnanomolar Heavy Metal Analysis, X-Ray Absorption Spectroscopy, and Surface Complexation Modeling. *Chemosphere* **2024**, *363*, 142766. [CrossRef]
45. Lai, L.; Liu, X.; Ren, W.; Zhou, Z.; Zhao, X.; Zeng, X.; Lin, C.; He, M.; Ouyang, W. Efficient Removal of Sb(III) from Water Using β-FeOOH-Modified Biochar:Synthesis, Performance and Mechanism. *Chemosphere* **2023**, *311*, 137057. [CrossRef] [PubMed]
46. Li, R.; Cao, X.; Fan, X.; Shi, J.; Meng, B.; Zhang, J.; Wang, Y.; Du, J.; Deng, X.; Zheng, C. Study of the Factors Influencing the Adsorption of Heavy Metal Pollutants in Water by Activated Carbon Gel Particles. *J. Environ. Eng.* **2024**, *150*, 04024024. [CrossRef]
47. Leng, Y.; Guo, W.; Su, S.; Yi, C.; Xing, L. Removal of Antimony(III) from Aqueous Solution by Graphene as an Adsorbent. *Chem. Eng. J.* **2012**, *211–212*, 406–411. [CrossRef]
48. Wang, H.W.; Li, X.-Y.; Li, W.H.; Sun, Y.J. Effects of pH and Complexing Agents on Sb(V) Adsorption onto Birnessite and Ferrihydrite Surface. *Huan Jing Ke Xue* **2017**, *38*, 180–187.
49. Zhang, C.; Jiang, H.; Deng, Y.; Wang, A. Adsorption Performance of Antimony by Modified Iron Powder. *RSC Adv.* **2019**, *9*, 31645–31653. [CrossRef]
50. Zhou, S.; Jiao, Y.; Zou, J.; Zheng, Z.; Zhu, G.; Deng, R.; Wang, C.; Peng, Y.; Wang, J. Adsorption of Sb(III) from Solution by Immobilized Microcystis Aeruginosa Microspheres Loaded with Magnetic Nano-Fe_3O_4. *Water* **2024**, *16*, 681. [CrossRef]
51. Yang, J.H.; Li, C.; Xie, S.B.; Yang, B.; Wei, B.; Tian, Z. Preparation of Fe-Mn layered double hydroxides and its adsorption behavior of Antimony(III) from wastewater. *Fhclxb* **2022**, *39*, 3871–3881.
52. Qi, P.; Luo, R.; Pichler, T.; Zeng, J.; Wang, Y.; Fan, Y.; Sui, K. Development of a Magnetic Core-Shell FeO@TA@UiO-66 Microsphere for Removal of Arsenic(III) and Antimony(III) from Aqueous Solution34. *J. Hazard. Mater.* **2019**, *378*, 120721. [CrossRef] [PubMed]
53. Li, X.; Dou, X.; Li, J. Antimony(V) Removal from Water by Iron-Zirconium Bimetal Oxide: Performance and Mechanism. *J. Environ. Sci.* **2012**, *24*, 1197–1203. [CrossRef] [PubMed]
54. Yan, M.Q.; Yang, Y.; Yang, C.K.; Shi, H.X. Study on the Adsorption and Removal of Antimony by Biochar Supported Mn Doped Nano Fe_3O_4. *Technol. Water Treat.* **2024**, *50*, 41–46.
55. Wang, L.; Wang, J.Y.; Wang, Z.X.; He, C.; Lyu, W.; Yan, W.; Yang, L. Enhanced Antimonate (Sb(V)) Removal from Aqueous Solution by La-Doped Magnetic Biochars. *Chem. Eng. J.* **2018**, *354*, 623–632. [CrossRef]

Disclaimer/Publisher's Note: The statements, opinions and data contained in all publications are solely those of the individual author(s) and contributor(s) and not of MDPI and/or the editor(s). MDPI and/or the editor(s) disclaim responsibility for any injury to people or property resulting from any ideas, methods, instructions or products referred to in the content.